Hindawi
Advances in Materials Science and Engineering
Volume 2021, Article ID 1031517, 14 pages
https://doi.org/10.1155/2021/1031517

Research Article

Development Research on Integrating CNC Machine Tool with Plasma for Online Surface Heat Treatment

Shao-Hsien Chen [1] and Bo-Ting Wang [2]

[1] *The Graduate Institute of Precision Manufacturing, National Chin-Yi University of Technology, No. 57, Sec. 2, Zhongshan Rd., Taiping Dist., Taichung 41170, Taiwan*
[2] *Department of Mechanical Engineering, National Chin-Yi University of Technology, No. 57, Sec. 2, Zhongshan Rd., Taiping Dist., Taichung 41170, Taiwan*

Correspondence should be addressed to Shao-Hsien Chen; e6036@ncut.edu.tw

Received 28 June 2021; Revised 27 August 2021; Accepted 7 September 2021; Published 16 October 2021

Academic Editor: Fuat Kara

Copyright © 2021 Shao-Hsien Chen and Bo-Ting Wang. This is an open access article distributed under the Creative Commons Attribution License, which permits unrestricted use, distribution, and reproduction in any medium, provided the original work is properly cited.

In this study, the plasma was integrated with a lathe, and the online heat treatment was performed to achieve mechanical strength and hardness, to reduce the machining process and handling. However, for online heat treatment of cast iron FC25, it is important to study the parameters of the lathe and plasma, and the research method is used eventually to optimize the process and reduce the machining cost and machining error. The variable factors in the surface online real-time heat treatment are spindle speed, feed rate, and current, and the objective function is the hardness of mechanical properties. In the screening experiment, the interaction of factors was discussed using a full factorial experiment. The Central Composite Design was combined with the Lack-of-Fit test for the optimization experiment, and the R^2 coefficient was used to determine whether the regression model is appropriate. The optimum parameters were derived from the contour diagram and response surface diagram. The experimental results show that the significant factors include spindle speed, feed rate, and current and the optimum parameters include spindle speed of 168 rpm, feed rate of 0.068 mm/rev, and current of 86 A. The experimental results of optimum parameters show that the surface hardness is increased from 306 HLD to 806 HLD and the surface hardening effect is enhanced by 163%, so the online real-time heat treatment equipment has the best hardening effect.

1. Introduction

Under the large output value of the automobile industry, the demand for automobile metal plates increases gradually. The automobile metal plates are machined by stamping, bending, and stretching, so the machining or handling of the large-sized metal plate molds takes a lot of time. The metal plate molds are high-cost processed bests. To prolong the service life of molds, surface heat treatment is required during machining to implement surface hardening. The flame treatment is mostly used at present. This study will use plasma in the lathe (CNC lathe) to study parameters, aiming at online real-time surface heat treatment, to achieve mechanical properties and surface hardening, and can reduce the processing procedure, as shown in Figure 1. This study is a quantitative experiment, and the width and diameter of the workpiece were 20 mm and 40 mm, respectively. Li et al. [1] used high energy density of plasma for quench hardening of tank parts. The result showed that the part surface hardness was higher than HRC55, the deformation was 0.01 mm, the depth of hardening was 0.02 mm, applicable to partial hardening, the result was best, and the service life of parts was prolonged. For long-term operation and maintaining the stability of the plasma machine, Zhou [2] designed a plasma control system, and the machine values were visualized. This system extracted the current and voltage variations in the experiment, it was used in multiple steel products for surface treatment, and the average surface hardness was HRC52~62. Cui et al. [3] used the plasma surface treatment

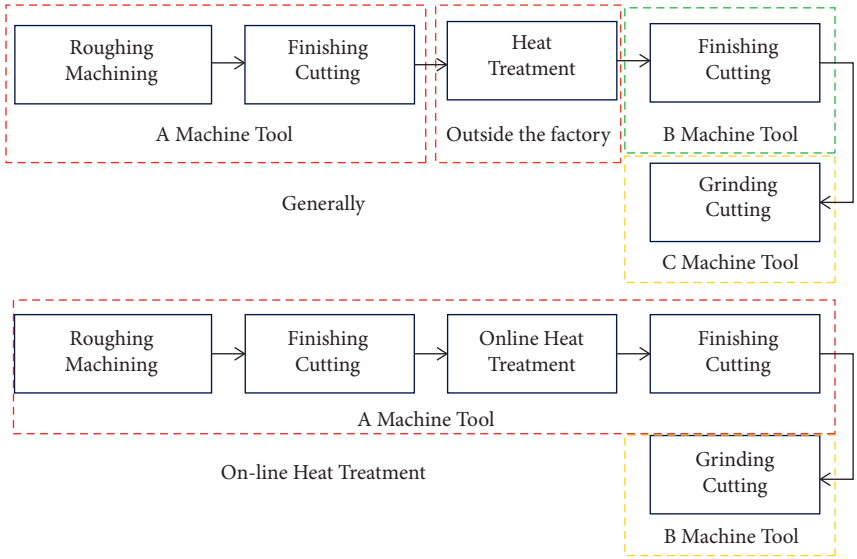

Figure 1: Comparison of general processing and online hot processing.

technique for enhancing the gear hardness, the result showed that the plasma surface treatment enhanced the gear surface hardness and wear resistance, and the gear size and tooth shape would not be deformed by the treatment process. The surface hardening value was 750~850HV, 15~20 times of the material hardness before treatment, and the hardened layer was 0.15~0.3 mm thick. Yang [4] performed mathematical derivation for the theoretical basis of plasma arc surface quenching temperature simulation and built a plasma heat source model. The analytical software ANSYS was used for analyzing the distribution of the overall temperature field of quenching, and the arc power, feed rate, plasma head nozzle hole diameter, workpiece preheating, and the parameters of different cooling methods were tested. The validation experiment was performed at last. The experimental results matched the software analysis results. The author in [5] used finite element analysis to study the distribution patterns of temperature field and stress field of 40Cr steel product and used X-ray stress detector to test the residual stress after quenching of 40Cr steel product. In terms of the plasma quenching cooling method, the workpiece generates stress by its heat transfer, and this stress is residual compressive stress [5]. The fatigue failure of the workpiece surface can be improved effectively according to analysis, but the workpiece is likely to a flaw. The result showed that the nozzle diameter and output current had a relatively greater influence on residual compressive stress. The laser was used to treat the surface of AISI 4140 intermediate-carbon chrome-molybdenum steel, and the improved mechanical properties were analyzed after treatment. The result showed that the metallographic structure was changed from materials ferrite and pearlite into plumose martensite structure, the surface hardness was increased by 238% from Hv237 to 771, the material yield strength was 94 kg/mm^2 and 125 kg/mm^2 after laser processing, the amplitude was 33%, and the tensile strength was increased by 14% from 118 kg/mm^2 to 139 kg/mm^2 [6]. The laser was used to treat the surface of AISI 4140 chrome-molybdenum steel, M2 tool steel, and a new type of steel KDIIS. The experimental results showed that the surface hardness of AISI 4140 was Hv750 after laser surface treatment, that of M2 tool steel was Hv1200, and that of a new type of steel KDIIS was Hv1200. In the experimental process, the temperature rose rapidly to austenitizing temperature and dropped rapidly, and the carbon atoms in the material had no time to generate cementite. The BCT crystal was obtained, and the lattice was distorted, so the hardness was quite high, and it was a martensite structure [7].

After laser surface treatment of SK3, SK5, SK7, and SKD61 steels, the surface hardening and metallography show variation. The case hardness of carbon tool steel SK3 was Hv910, the case hardness of SK5 was Hv900, the case hardness of SK7 was Hv950, and the case hardness of die steel SKD61 was Hv1100. The main hardening condition of dies steel SKD61 depended on whether the carbides were dissolved in the base austenite or not. The structure was divided into three parts after quenching, including hard zone, transition zone, and substrate zone. The distribution of carbides in the hard zone decreased obviously because the high temperature of laser surface treatment dissolved surface carbides in the base, the hard zone had the highest hardness value, and the transition zone and substrate zone were tempered martensite structure and fine carbides [8–10].

After laser surface treatment of AISI-1045, AISI-4140, and AISI- 4340, the increase of surface hardened the mechanical properties. The experimental results showed that the hardness of medium carbon steel AISI 1045 was increased from 316HV to 755HV, and the surface hardness was increased by 138%. The hardness of chrome-molybdenum steel AISI 4140 was increased from Hv396 to Hv801, and the surface hardness was increased by 102%. The hardness of nickel-chromium-molybdenum steel AISI 4340

was increased from 441HV to 833HV, and the surface hardness was increased by 88%. The depth of hardening of medium carbon steel AISI 1045 was 0.85–1.45 mm, the depth of hardening of chrome-molybdenum steel AISI 4140 was 0.96–1.65 mm, and the depth of hardening of nickel-chromium-molybdenum steel AISI 4340 was 0.91–1.88 mm. According to the above references, laser hardening was mostly used. This study will combine plasma hardening with response surface methodology to study parameter optimization, and the hardening effect can be achieved at a lower cost, but there is no related study at present [11, 12]. Cryogenic treatment is applied to improve the properties of materials, and the cryogenic treatment increased the thrust force during the drilling operation [13]. The grain refinement was observed in the microstructure of the cutting surface although grain growth was also observed due to a rise in temperature [14]. Reviewing data published in the literature reveal that the phenomenon reported in this paper has not surface hardening of the plasma and lathe integration observed.

The objectives of this study include (1) evaluating the hardening efficiency of plasma heat treatment, (2) comparing the effects of experimental parameters current, spindle speed, and feed on hardening results, and (3) investigating the optimization and verification of plasma heat treatment parameters.

2. Principle and Method

The heat source model and parameters shall be determined before the test because the selection of an equivalent plasma heat source mathematical model will directly influence the heat distribution of the concentrated heat source. When the concentrated heat source works [16], the temperature distribution on the metal surface close to the center of the concentrated heat source depends on the heat source type, and the temperature distribution on the metal surface far from the center of the heat source is determined by the thermophysical property of metal material. The common concentrated heat sources include point line and surface heat sources [17, 18]. It is a Gaussian heat source during plasma arc quenching [15, 19]. Figure 2 shows the distribution of heat flux of Gaussian heat source, the heat flow follows Gaussian distribution, and the Gaussian heat source function is expressed as follows:

$$q(r) = q_m \exp\left(-kr^2\right). \tag{1}$$

In equation (1), $q(r)$ is the heat flux density (W/m^2) at radius r; q_m is the heat flux density (W/m^2) at the center of arc column; r is the distance (m) from the center point of plasma heat source to any point of the hot zone; and k is the Gaussian heat source distribution curve shape coefficient (m^{-2})

The effective power of plasma for heating workpiece is as shown in equation (2); the experimental parameters are V is the plasma voltage, I is the plasma current value, and η is the plasma thermal efficiency [20–22].

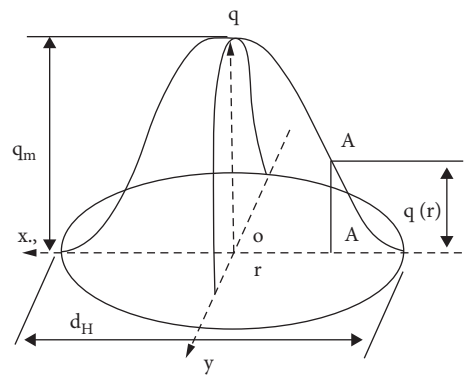

Figure 2: Gaussian heat flux distribution [15].

$$q = 0.24 \times \eta \times I \times V. \tag{2}$$

3. Experimental Equipment and Planning

The experimental workpiece is FC25 gray cast iron in this study, which has the best casting property, cutting characteristic, and wear resistance. The metallographic structure of the material comprises ferrite + pearlite + flake graphite. The graphite content in the structure can achieve a self-lubricating effect. This study uses DC plasma heat source output to simulate immediate surface heat treatment after lathe finish machining. As the material metallography shall be analyzed after hardening, cutting machining is required, preventing the heat generated in the cutting process from changing the end product surface metallography. Therefore, this study uses a workpiece in the outside diameter of 40 mm and thickness of 20 mm, and the material workpiece is prepared before the experiment.

A single-spindle lathe as an experimental carrier and a hollow cylinder are used for the experiment. The lathe spindle controls the spindle speed (rpm), and the plasma gun head is fastened to the cutting tool rest to control the feed rate (mm/rev) so as to uniformly heat up the material surface. The plasma device for the experiment is of transferred arc type, numerically controlling the movement, making the plasma gun head approach the workpiece to form a loop, and generating an electric arc for heating. In terms of heat source output, the current (A) controls the output of heat source energy magnitude. The experimental configuration is shown in Figure 3. The flow chart of the experimental analysis and model establishment of this research is shown in Figure 4.

The material used in this study is cast iron FC25. The mechanical properties and components are shown in Tables 1 and 2, and the diameter, thickness, and hole of the workpiece were 40 mm, 20 mm, and 12 mm, respectively, and are shown in Figure 5.

The experimental procedures and steps of this research are as follows:

Step 1. Establish the relationship between plasma power and heat treatment temperature

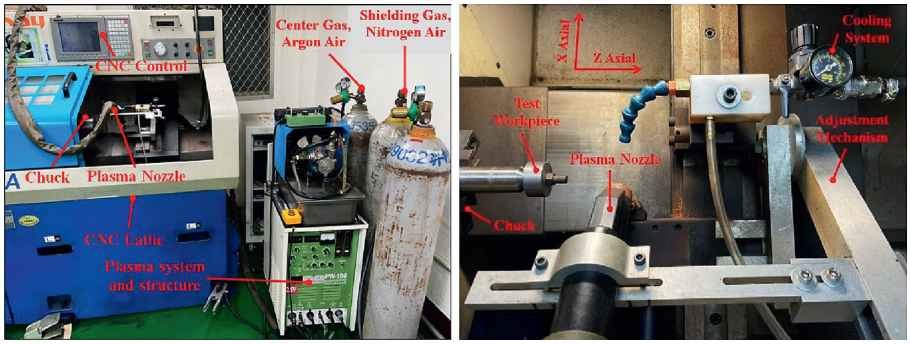

Figure 3: Lathe and plasma experiment equipment and system.

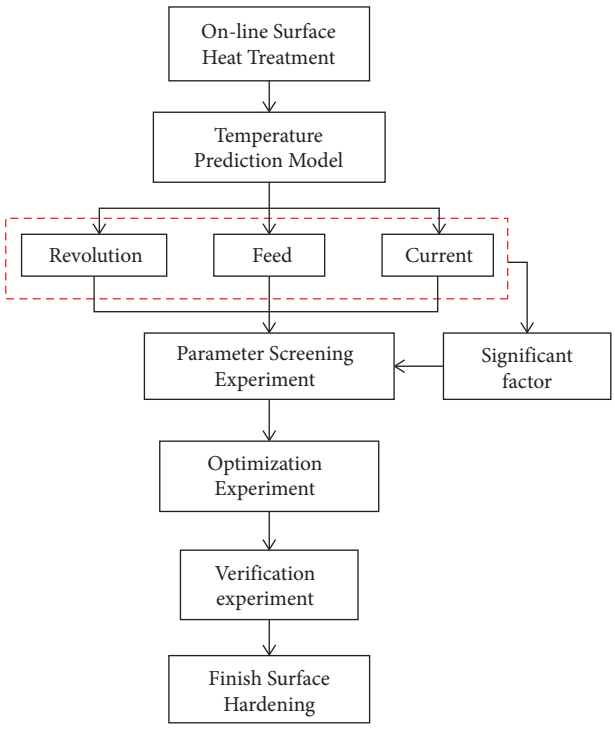

Figure 4: Experimental flowchart and process.

Table 1: FC25 chemical composition (%).

	C	P	Si	Mn	S	Ti
FC25	3~3.3	≤0.12	1.65~2.05	0.7~1.1	≤0.12	≤0.05

Table 2: FC25 mechanical properties.

	Tensile strength	Extension (%)	Reduction of area (%)	Hardness
FC25	830 N/mm^2	≥ 20	≥ 45	306 HLD

Step 2. Full factorial experiment is used for temperature model establishment and prediction

Step 3. The predictive model results obtained in this study confirm not only the physical phenomena but also the verification experiment, and the experiment is repeated for five times.

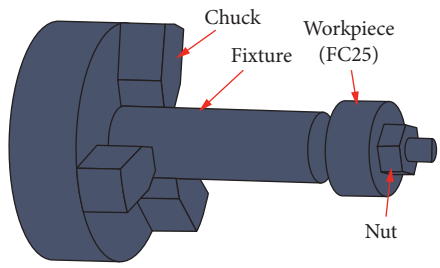

Figure 5: Experimental workpiece clamping.

Step 4. The optimized model is established and experiment is verified, mainly observing hardness and metallographic structure.

4. Results and Discussion

4.1. Relationship between Temperature and Material

4.1.1. Temperature Prediction Model Building. This study mainly uses plasma for sudden heating of the material to generate cementite and steatite deposition, to harden the surface. Therefore, the temperature prediction model shall be built before research to confirm the current; the full factorial experiment is used in temperature prediction modeling experiment; the parameter setting experiment conditions are as follows: the outside diameter of FC25 gray cast iron is 40 mm, the heating distance is 50 mm, the estimated temperature rise is 100°C~300°C, the established parameters are shown in Table 3, parameter setting refers to equation (2), and the voltage, current, and plasma thermal efficiency of the parameter were $V = 220$ V, $I = 40$ A~60 A, and $\eta = 0.23$, respectively.

The experimental parameters are designed by using RSM. The experimental results are discussed below. When the feed rate is fixed at 0.42 mm/rev, the spindle speed is 175~225 rpm, and the current is 50~60 A, the temperature rises as the current increases; the current is proportional to the thermal power according to equation (3); the maximum temperature difference is 25%. In terms of spindle speed, the higher the spindle speed is, the shorter the single-point heating time is, so the temperature effect is inversely proportional to the spindle speed, and the maximum temperature difference is 18%. When the current is fixed at 40 A, the spindle speed is 175~200 rpm, and the feed rate is

Table 3: Experimental factors and levels.

	Level I	Level II	Level III
(A) Spindle speed (rpm)	175	200	225
(B) Feed rate (mm/rev)	0.3	0.36	0.42
(C) Current (A)	40	50	60

0.3~0.42 mm/rev, the temperature drops as the spindle speed increases; because the single-point heating time is shorter, the temperature is lower, and the maximum temperature difference is 10%, as shown in Figure 6. The lower the feed rate is, the higher the temperature is, and the maximum temperature difference is 22.5%. When the spindle speed is fixed at 225 rpm, the current is 40~60 A, and the feed rate is 0.3~0.36 mm/rev, the higher the current is, the higher the temperature is. The current is proportional to the thermal power according to equation (2), and the maximum temperature difference is 60.4%.

The temperature prediction model is built by using temperature measurement after the test. The partial least squares method and regression (PLSMR) and least square method and regression (LSMR) are compared. The parameters are designed by using RSM. P value <0.05 and R^2 value > 0.9 in analysis. The result of PLSMR is shown in Figure 7. It is observed that the current value is a significant factor, the order of contributions is current > feed > spindle speed, and the regression prediction model is expressed as the following equation:

$$\text{Temp} = 231.5 - 0.621N - 333.1F + 3.454I. \quad (3)$$

When the LSMR is used that the experimental significance level $\alpha = 0.05$ and F value = 50, $F > F$ (0.05, 4, 2), the null hypothesis is rejected. The test coefficient $R^2 = 0.9709$ means 97.09% of the total variance in the model can be explained by the independent variable, and the regression model has high fitness, as shown in Figure 8. It is observed that the current value is a significant factor, the order of contributions is current > feed > spindle speed, and the regression prediction model is expressed as the following equation:

$$F = \frac{422.5}{191} = 221 < F_{(0.05,4,2)} = 19.2468. \quad (4)$$

4.1.2. Temperature Model Verification. Five groups of arbitrary parameters will be used for temperature validation after modeling. The temperature parameters are shown in Table 4. The predicted and experimental values are analyzed. The model verification uses MAPE (mean absolute percentage error) as a measurement indicator. The MAPE of the PLSMR model is 0.5935%, and the MAPE of the PLSMR model is 1.335%, so the PLSMR has higher accuracy, as shown in Table 5. However, both of the estimation methods are in the permissible range, and the results are shown in Table 6.

4.2. Influence of Different Parameters on Material Properties. The influence of different spindle speeds, feed rates, and current values on material properties is analyzed, the spindle speed is 200~300 rpm, the feed rate is 0.1~0.2 mm/rev, and the current value is 60~80A. Different parameters correspond to different workpiece single-point action thermal effects, so the material properties are analyzed and discussed, aiming at the material hardness and metallographic structure changes. The relationships between different parameters and mechanical properties are described below.

4.2.1. The Influence of Spindle Speed and Feed on Material Hardness. The influence of different spindle speed and feed rates on the hardness of mechanical properties is mainly the influence of operative temperature at a material single point, when the plasma power is fixed at I = 80 A, as shown in Figure 9; the hardness value is relatively higher when the spindle speed is lower because the workpiece spindle speed directly influences the heating time. When the feed rate is 0.1 mm/rev, the workpiece spindle speed is adjusted from 300 rpm to 200 rpm and the hardness value is increased by 35.4%. The influence of feed rate on hardness is observed in this experiment. The lower the feed rate is, the higher the hardness value is, and the first cause is the single-point heat source action time. When the workpiece spindle speed is 200 rpm, the feed rate is adjusted from 0.2 mm/rev to 0.1 mm/rev and the hardness value is increased by 69.3%.

When the plasma current is reduced to I = 60 A, the spindle speed is $N = 200\sim300$ rpm and the feed rate is $F = 0.1\sim0.2$ mm/rev. The fundamental purpose is to heat the workpiece uniformly to achieve a hardening effect; when the spindle speed is adjusted from 300 rpm to 200 rpm, the hardness value is increased by 19.6%. When the workpiece spindle speed is 200 rpm, the feed rate is adjusted from 0.2 mm/rev to 0.1 mm/rev and the hardness value is increased by 34%. According to the aforesaid data, the longer the unit residence time is, the higher the relative hardness is. Under variable plasma current, the higher the current is, the more obvious the relative hardness is.

4.2.2. Relationship of Different Current Values to a Hardness Value. When the feed rate is fixed, the effects of different spindle speed and plasma current values on material hardening and variation are observed. When the constant spindle speed is $N = 200$ rpm, the current value is increased by 25% from I = 60 A to I = 80 A and the hardening effect is increased by 27.8%. When the constant spindle speed is $N = 300$ rpm, the hardening effect is increased by 18.3%. When the current value is I = 80 A, the spindle speed is increased by 33% and the hardening effect is reduced by 35.4%. Therefore, the higher the spindle speed is, the worse the hardening effect is, as shown in Figure 10. When the spindle speed is fixed, the effects of different feed rates and plasma current values on material hardening and variation are observed. When the feed rate $F = 0.1$ mm/rev, the current value is increased by 25%, the hardening effect is 27%, and then the feed rate is increased to $F = 0.2$ mm/rev and the hardening effect is 8.9%. Therefore, the higher the feed rate is, the worse the hardening effect is. When the current value is I = 80 A, the feed rate is increased by 50% and the hardening effect is reduced by 69.3% because under different

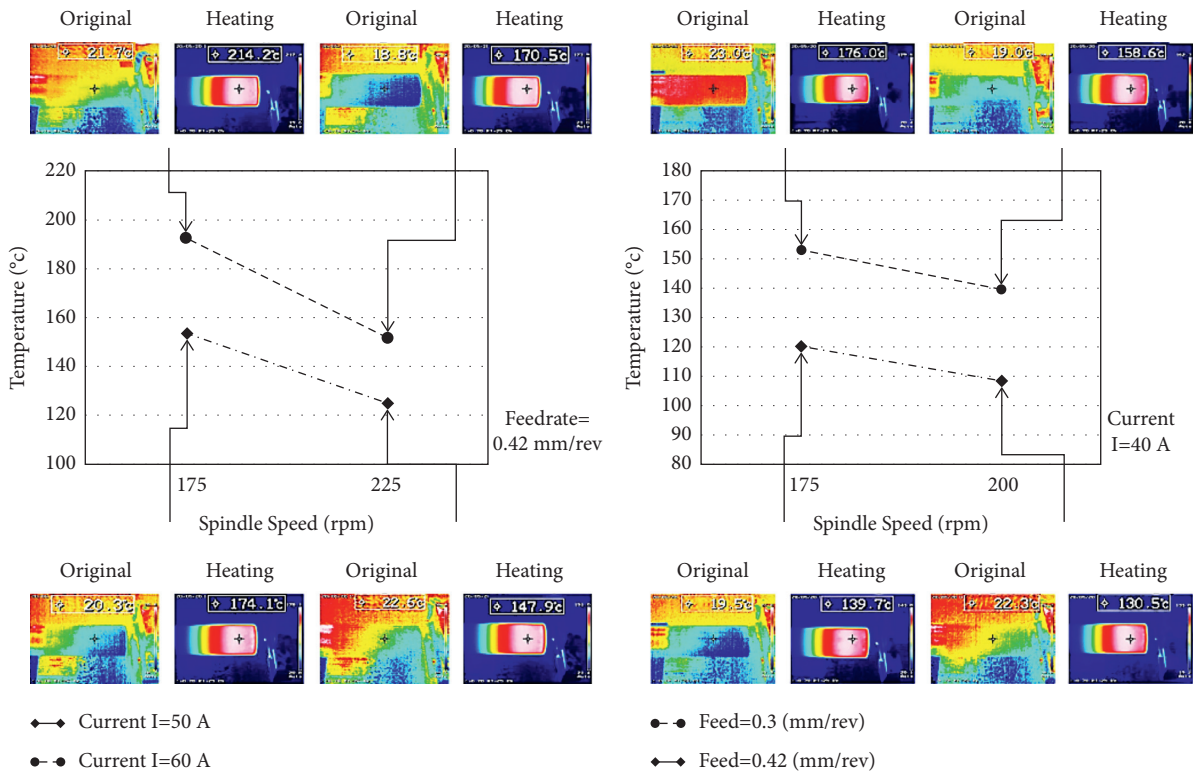

Figure 6: Relationship of different spindle speed and temperature.

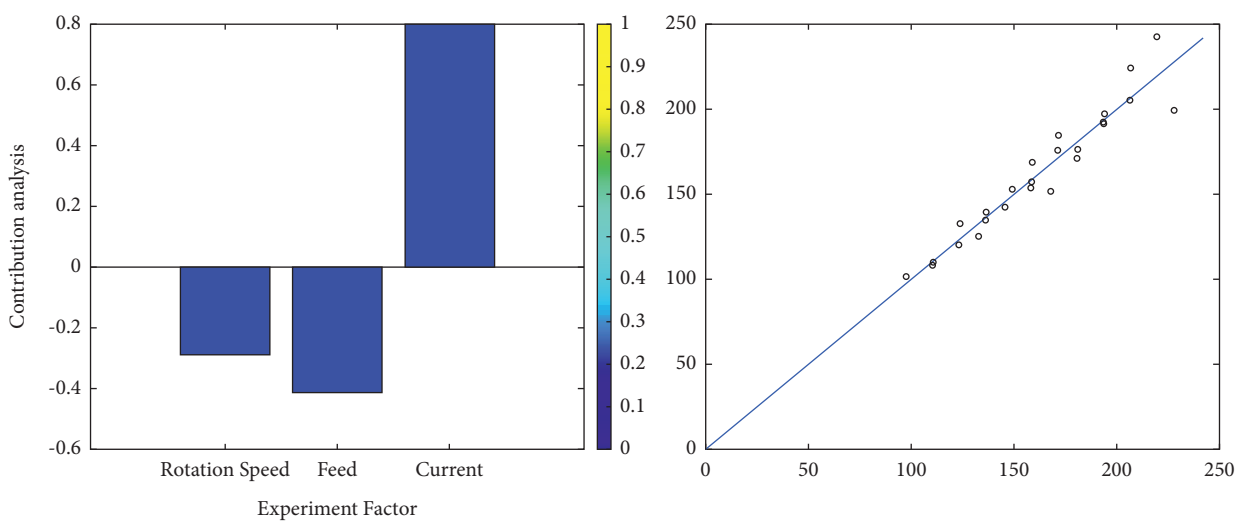

Figure 7: Partial least squares method and regression analysis chart.

parameters and temperatures, the experimental material produces different precipitates, and the final hardness value is influenced, as shown in Figure 9.

4.2.3. Description of Experimental Metallographic Structure. In the online heat treatment process, the mechanical parameters influence the temperature, leading to the hardening effect, and the influence on the hardening effect is closely bound up with the material structure, so the internal change is observed by using metallographic structure. The silicon content of 1.0~2.0% in the material presents the pearlite structure, the silicon can change the free carbon in the casting process into graphite crystal, and the cementite generation is reduced. When the graphite content in the structure increases, the texture is relatively soft and easy to cut. The amount of silicon content results in different crystals of graphite. During molding, the iron element and carbon element perform chemical action due to the high temperature inside cast iron so that the cementite is generated. The cementite has a hard and brittle texture, increasing the difficulty in subsequent material processing. To

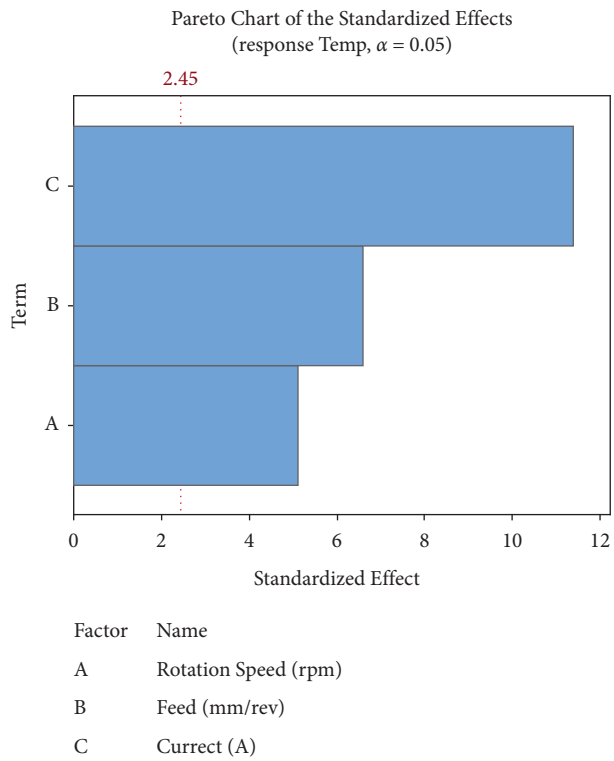

Figure 8: Least square method and regression analysis chart.

Table 4: Validation experiment parameter list.

Experimental parameter	Spindle speed (rpm)	Feed rate (mm/rev)	Current (A)
Group 1	213	0.33	45
Group 2	213	0.39	45
Group 3	188	0.33	55
Group 4	188	0.39	55
	188	0.39	45

Table 5: Prediction model analysis and comparison.

	Actual	Forecasted (LSMR)	Absolute percent error	Forecasted (PLSMR)	Absolute percent error
1	143.8	146.13	1.62	144.73	0.65
2	124.7	126.15	1.16	124.75	0.038
3	195.7	196.20	0.25	194.80	0.46
4	173.5	176.21	1.56	174.81	0.76
5	138.8	141.67	2.07	140.27	1.06
MAPE			1.34		0.59

prevent this problem, an amount of silicon is added to the casting process, and the carbon element is changed into graphite, to reduce the cementite generation. The ferrite is separated from the cementite during cooling, so a lot of ferrites adhere to the graphite crystals.

When the spindle speed $N = 300$ rpm, feed rate $F = 0.1$ mm/rev, and current value $\mathrm{I} = 80$ A, the measured hardness is 479 HLD, higher than the material surface hardness by 57%. As Figure 11 shows that most of the ferrite structure is changed into pearlite, a little graphite carbide is separated nearby the graphite crystal branches.

When the spindle speed $N = 200$ rpm, feed rate $F = 0.1$ mm/rev, and current value $\mathrm{I} = 80$ A, the experimental measurement result is 613 HLD, higher than the material surface hardness by 100%, and there is no obvious martensite feature in the structure, so the substrate is transformed from pearlite into pearlite + austenite eutectic. The experimental temperature has reached the transformation point, but the duration is too short to transform all structures, leading to this eutectic phenomenon. The heated graphite and the Fe element in the material have a chemical change to separate cementite,

Table 6: Validation experiment measurement results.

	Original temperature	Temperature after heating
1	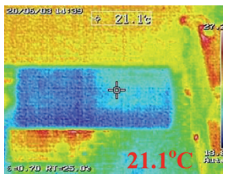	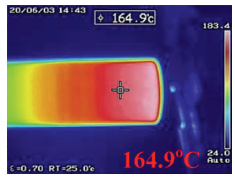
2	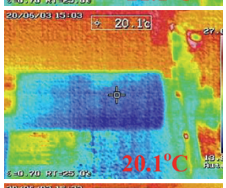	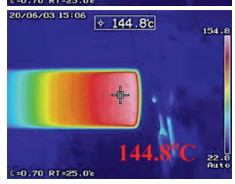
3	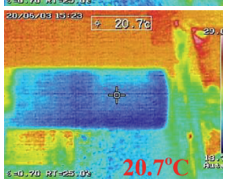	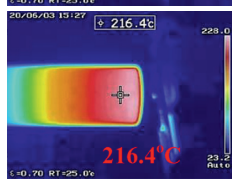
4	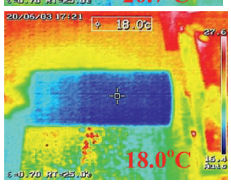	
5	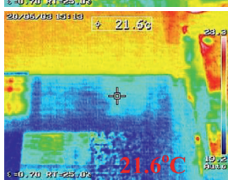	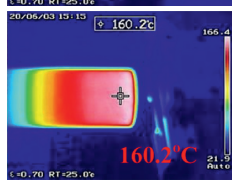

and it is observed that the original graphite crystal branches have been replaced by cementite.

The cast iron contains phosphor element; when the phosphor element is solidified again at a high temperature, this kind of iron phosphide is called steatite. The scattered white dots in Figure 10 are steatite, the hardness of steatite next to cementite, the wear resistance can be enhanced, and the heat resistance can be improved [23, 24]. In the metallograph diagram, the increase of hardness and brittleness will cause increase in cutting power and vice versa.

To fully melt the graphite, a long heating time is required, and the temperature shall be maintained, to destroy the graphite crystal appearance. The graphite precipitates cementite out, but the shape is the same as the graphite crystal because the heating time is too short.

4.3. Material Hardening Optimization Experiment. In the online hardening heat treatment process, the temperature has an obvious effect on material structure, and the material structure change can induce mechanical hardening. In Stage 2, the experimental significant factors are used for full factorial Central Composite Design. The experimental parameters adopt 3 factors and 5 levels. The experimental sequence is performed using random numbers. The design of experimental parameters is shown in Table 7. After the experiment, the changed hardness of the material is used to measure and build the prediction model, and the LSMR is used for analysis.

In the first-order model Lack-of-Fit test, the Lack-of-Fit P-value of this model is $0.022 < \alpha = 0.05$, it is confirmed that this model cannot fit data, the Lack-of-Fit F value is $9.32 > F_{(0.05,11,4)}$, the null hypothesis is rejected, the R^2 coefficient is 86.55%, in the R^2 coefficient test, the value is relatively low, and the analysis is performed without eliminating second-order model existence.

$$F = \frac{1490.8}{159.8} = 9.32 > F_{(0.05,11,4)} = 5.96. \tag{5}$$

In the second-order model Lack-of-Fit test, the full factorial is used for analysis in Stage 1, the model Lack-of-Fit P-value is $0.284 > \alpha = 0.05$, there is no evidence for the failure in fitting data, the Lack-of-Fit F value is $1.856 < F_{(0.05,5,4)}$, the null hypothesis is not rejected, the R^2 coefficient is 98.32%, and the second-order model is more applicable than the first-order model.

$$F = \frac{296.6}{159.8} = 1.856 < F_{(0.05,5,4)} = 6.26. \tag{6}$$

In Stage 2, the coefficients in the quadratic term and interaction term are insignificant, meaning the terms have a slight influence on the hardness response variable in the experimental results, so the term with low contribution is deleted, and the ANOVA is performed after an adjustment.

$$F = \frac{369.2}{159.8} = 2.31 < F_{(0.05,8,4)} = 6.04. \tag{7}$$

In the adjusted second-order model Lack-of-Fit test, the Lack-of-Fit P-value of this model is $0.218 > \alpha = 0.05$, there is no evidence indicating that the model cannot fit data, the Lack-of-Fit F value is $2.31 < F_{(0.05,8,4)}$, the null hypothesis is not rejected, and the R^2 coefficient is 97.16%, meaning 97.16% of the total variance in the model can be explained by the independent variable.

The regression equation is as follows:

$$\begin{aligned} Y = {} & 1033 - 3.99A - 2828B + 6.94C + 0.0064A^2 \\ & + 10596B^2 - 26.7B * C. \end{aligned} \tag{8}$$

The regression prediction equation is built by using RSM, and the validation experiment shall be performed to check whether the model meets the standard or not. The validation experiment parameters are shown in Table 8~9, and three groups of experimental parameters are selected at random and substituted in the equation for validation. The experimental workpiece is measured five times, the average value is taken, and the maximum error is 2.01% according to experimental analysis and model verification. According to the aforesaid three groups of experimental results, the estimated values of the temperature prediction equation fall in the confidence interval, and the estimation ability is best

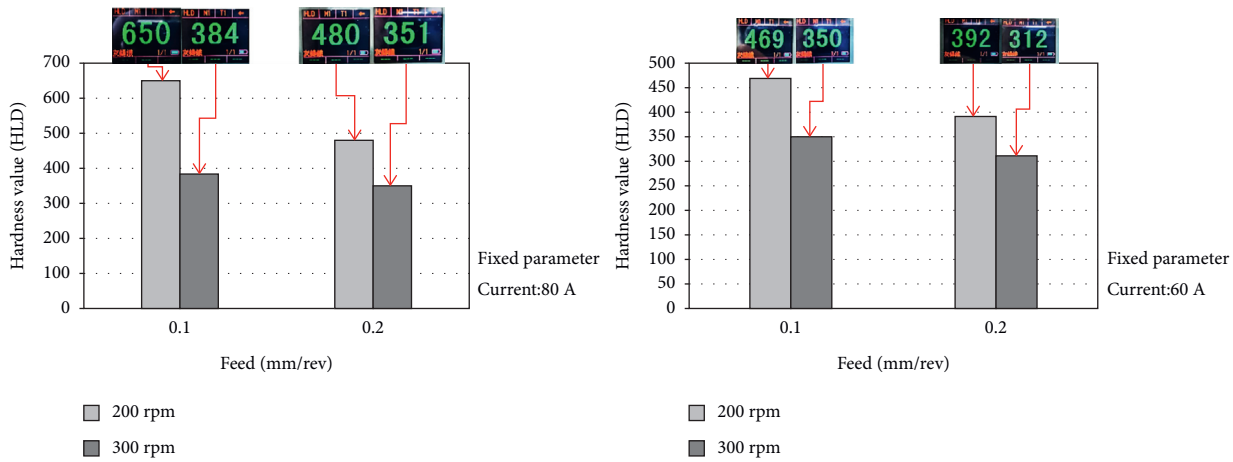

Figure 9: Relationship of different spindle speeds to a hardness value.

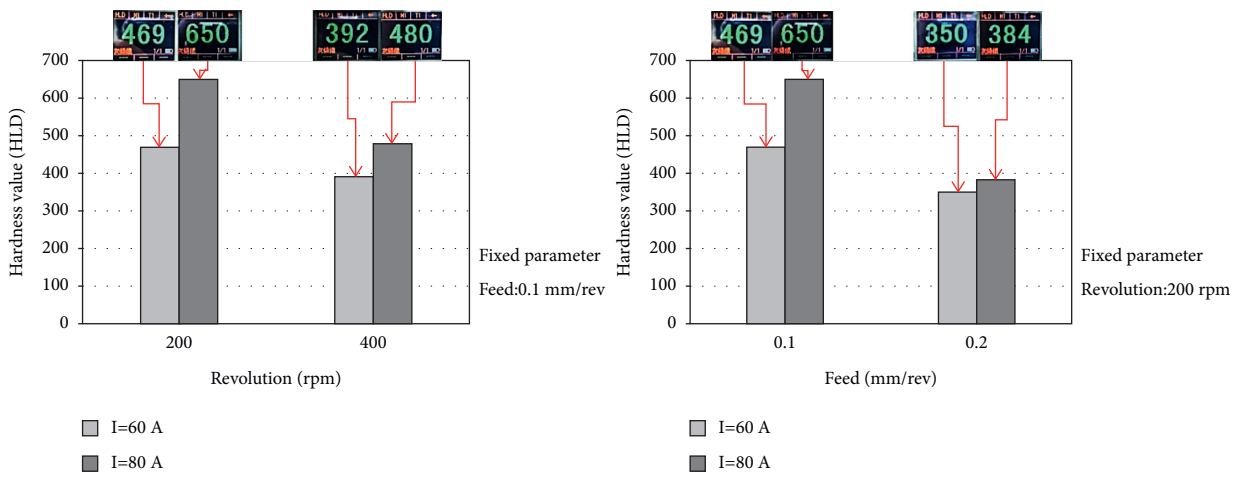

Figure 10: Relationship of different current values to a hardness value.

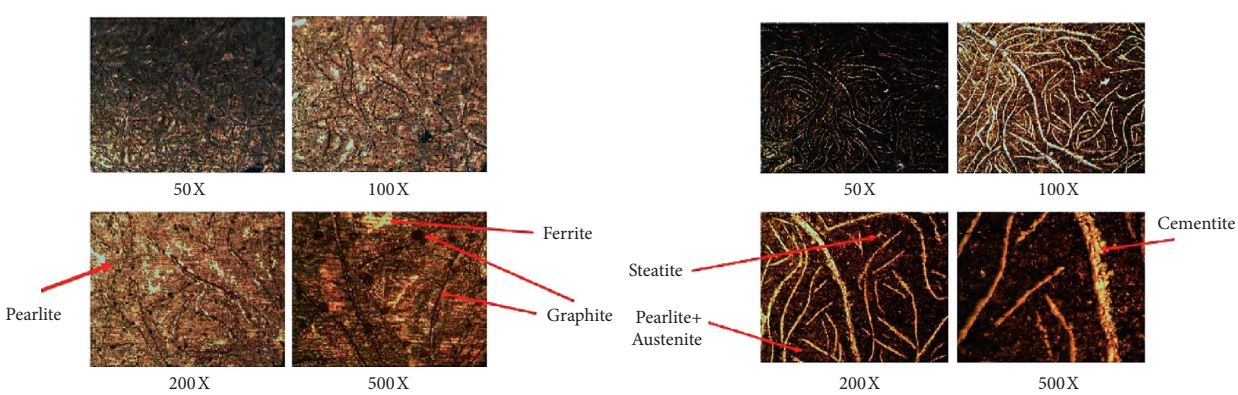

Figure 11: Metallograph diagram of Experiments 5 and 7.

Table 7: Optimization experiment factors and levels.

Factor level	1.633	1	0	−1	−1.633
Spindle speed (rpm) (A)	168	200	250	300	331
Feed rate (mm/rev) (B)	0.07	0.1	0.15	0.2	0.23
Current (A) (C)	64	60	70	80	86

Table 8: Validation experiment parameter list.

Experimental parameter	Spindle speed (rpm)	Feed rate (mm/rev)	Current (A)
Group 1	200	0.1	60
Group 2	250	0.15	70
Group 3	300	0.2	80

Table 9: Verification experiment result.

	Actual average HLD	Predicted HLD	Error (%)
Group 1	572	570	0.35
Group 2	451	455	0.88
Group 3	406	398	2.01

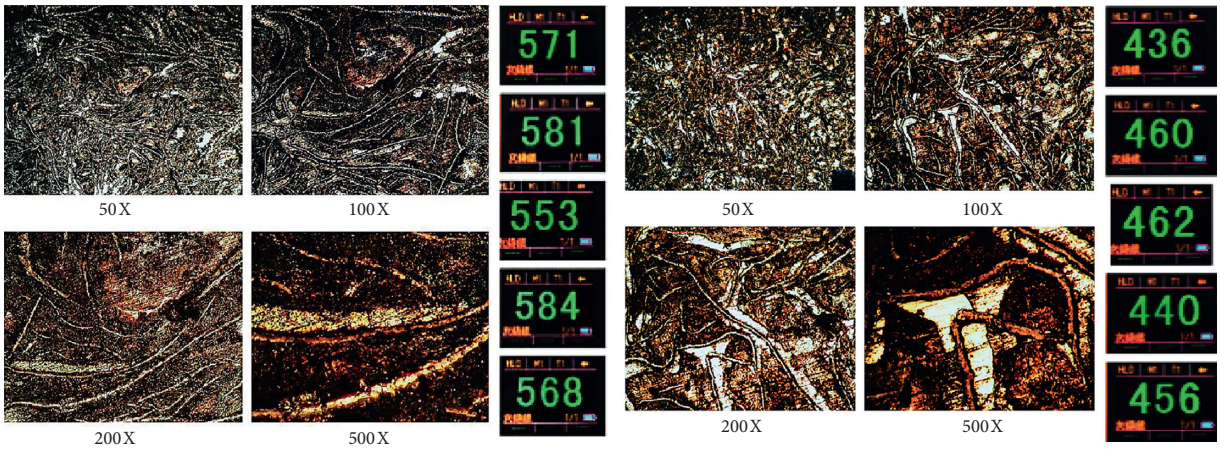

Figure 12: Metallograph diagram and hardness of validation Experiments 1 and 3.

[25, 26]. The three groups of metallographic structure are as shown in Figure 12.

4.4. Analysis and Validation of Optimum Parameters. According to analysis, the spindle speed, feed rate, and current can influence the temperature, and then the workpiece hardness and mechanical properties are influenced. According to the contour diagram of spindle speed and feed rate to surface hardness, when the current is fixed at $I = 70$ A, the lower the spindle speed and feed rate are, the better the material hardening effect is, and the results are shown in Figure 13. According to the contour diagram of feed rate and current value to surface hardness, when the spindle speed is fixed at $N = 250$ rpm, the higher the current is and the lower the feed rate is, the better the material hardening effect is, and the results are shown in Figure 14. According to the contour diagram of spindle speed and current value to surface hardness, when the feed rate is fixed at $F = 0.15$, the higher the current is and the lower the spindle speed is, the better the material hardening effect is, and the results are shown in Figure 15. Because the shorter the distance acting on the material per unit time is, the better the hardening effect is [27–29].

According to the contour diagrams, the lower the spindle speed and feed rate are and the higher the current is, the better the hardening effect is. The optimization parameter planning and design can refer to the contour diagrams. Figure 16 shows the optimization parameter design; when the spindle speed is 168 rpm, the feed rate is 0.68 mm/rev, and the current is 86 A, the hardening effect can be maximized.

Finally, the RSM is used to establish the optimal mechanical hardness for the validation experiment, the experimental results are shown in Table 10, the hardening effect is 806 HLD (61 HRC), the error between the experimental result and the optimum solution from the model is 4%, and the material hardness value is increased by 163%. The metallographic structure shows that the original flake graphite chemically reacts with peripheral ferrite due to the high temperature, and the cementite is precipitated (Fe_3C). Figure 17 shows that many white dots are steatite, the material contains phosphor element,

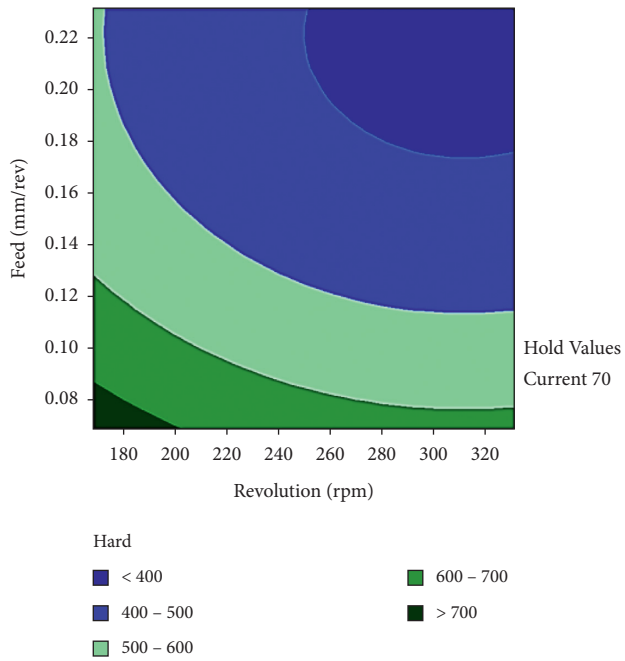

Figure 13: Contour diagram of spindle speed and feed rate to surface hardness.

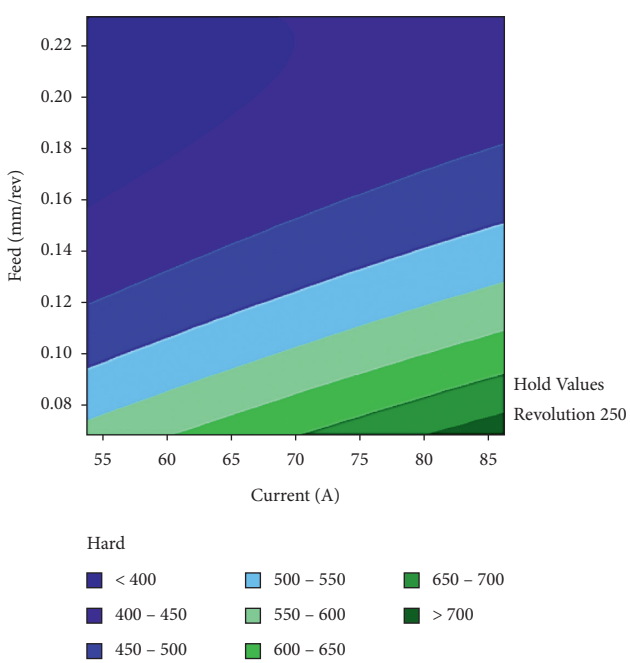

Figure 14: Contour diagram of feed rate and current value to surface hardness.

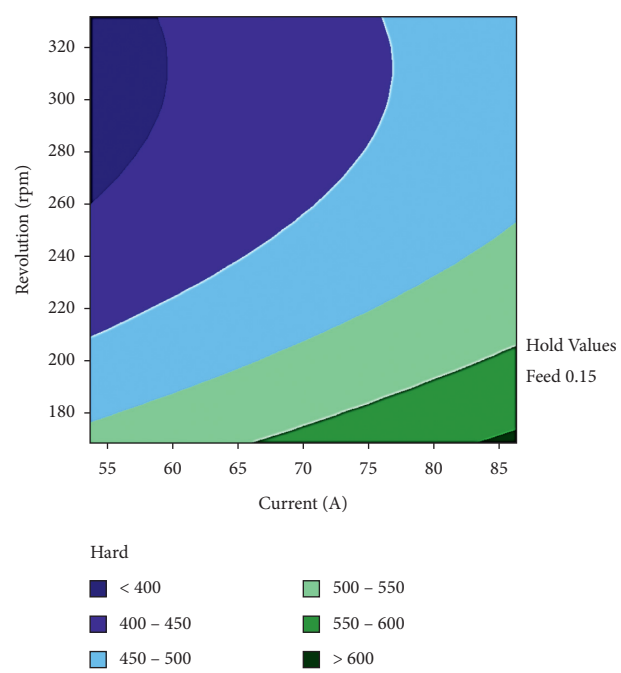

Figure 15: Contour diagram of spindle speed and current value to surface hardness.

iron element, and carbon element, which form the Fe-Fe_3-Fe_3p ternary eutectic at high temperature, and then the steatite structure is precipitated; the substrate is supposed to be pearlite + austenite mixture, so the increase in the hardness may result from the cementite and steatite in the structure [30]. It has cementite in the

Table 10: Experimental results of optimum parameters.

	Material hardness HLD	Optimal material hardness HLD
Response value	306	806

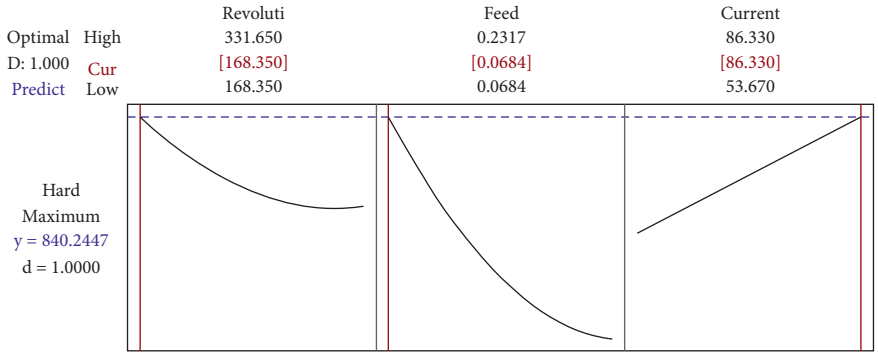

Figure 16: Optimum parameter design.

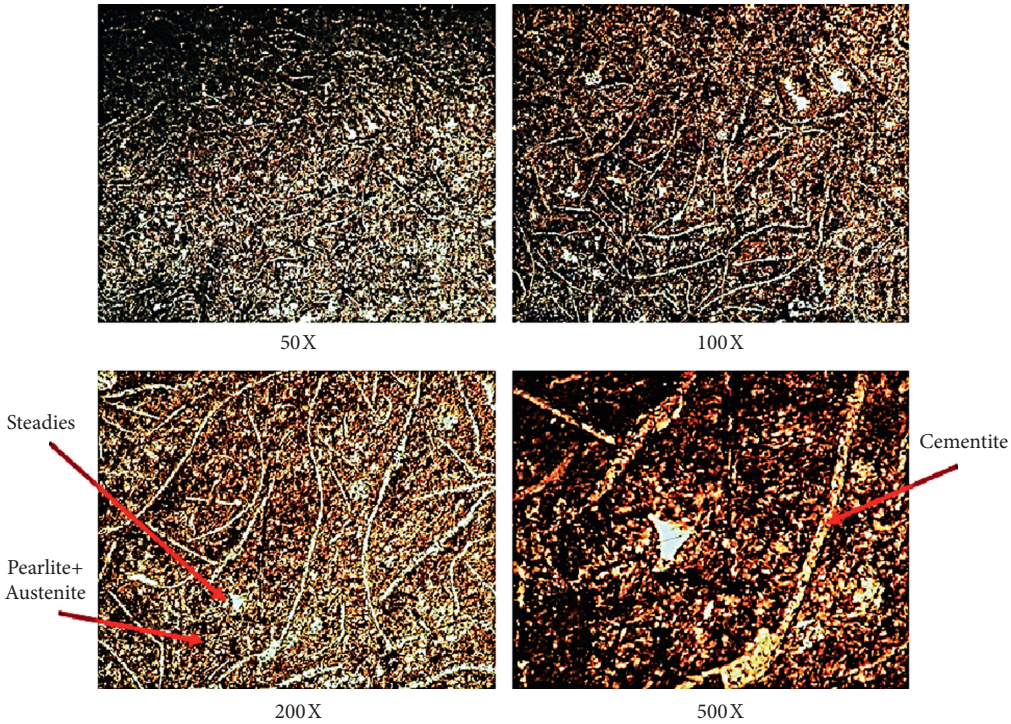

Figure 17: Metallograph diagram of optimum parameters.

metallograph diagram, and it has mechanical properties of higher hardness and brittleness, so the increase in cementite will cause increasing the cutting power and tool wear.

5. Conclusion

In the online heat treatment process, the method is used for process optimization and reducing the die cost. The

experimental equipment includes a DC variable frequency plasma welder and CNC lathe for simulating the surface heat treatment process after mold machining, and the actual effect of spindle speed, feed rate, and current factors on surface hardening is discussed. The RSM regression analysis model, ANOVA, Pareto chart, and Lack-of-Fit test statistics are used to discuss the interaction between significant factors and factors in the process. The design of the experiment is a full factorial experiment, and the Central Composite Design is combined with RSM, to discuss the factor-surface hardness contour diagram and optimum parameters, validating the effect of optimum parameters on enhancing surface hardness. This study is concluded as follows:

(1) According to the equation conversion and actual temperature rise measurement, the experimental machine thermal efficiency is 0.44, the temperature prediction model is built according to 27 groups of experimental results of a full factorial experiment, the model equation is validated by 95% confidence interval, and the actual temperature rises of five groups of validation experiment results fall in this interval.

(2) The temperature model MPAE is 1.36%, it is high accuracy prediction, the MAPE of temperature repeatability experiment is 1.41%, and it is high accuracy prediction.

(3) According to the screening experiment result, the spindle speed is reduced by 100 rpm, the surface hardness is increased by at most 31%, the feed rate is reduced by 0.1 mm/rev, the surface hardness is increased by at most 64%, the current is increased by 20 A, and the surface hardness is increased by at most 34%.

(4) The metallographic structure of the material is pearlite + ferrite + flake graphite; when the surface hardness is 479 HLD, most of the pearlite in the structure is dissolved in the base pearlite. When the surface hardness is 613 HLD, the flake graphite in the structure is changed into cementite structure and the cementite reacts with phosphor element to precipitate ternary eutectic steatite structure.

(5) The optimization experiment uses 20 groups of Central Composite Design, the significant factor relationships are current > feed rate > spindle speed, the model and equation are validated by 95% confidence interval, and the three groups of validation experiment results show that the average hardness values fall in this interval.

(6) According to the contour diagrams and response surface diagram, the optimum parameters are spindle speed of 163 rpm, feed rate of 0.068 mm/rev, and current of 86 A. The material processing hardening objective of optimum parameters is 839; according to the experimental results of optimum parameters, the experimental material is increased from 306 HLD to 806 HLD, the hardening effect is enhanced by 163%, and the error from the expected value is 4%. In our simulated heating experiment, the simultaneous movement of the spindle and the saddle causes the difficulty of temperature measurement technology, so the high temperature and speed do not consider the measurement. Future research will be focused on the plasma with water mist online surface heat treatment for quenching, because of increase in surface hardening effect [31].

Data Availability

The data required to reproduce these findings cannot be shared at this time as the data also form part of an ongoing study

Conflicts of Interest

The authors declare that they have no conflicts of interest.

References

[1] M. R. Li, J. Zhang, and Y. Sun, "Application of plasma arc quenching process on tank parts," *Journal of Shenyang University of Technology*, vol. 25, no. 1, 2003.

[2] Q. Zhou, *Development and Research of Plasma Surface Quenching Control System*, Master's degree thesis, Shenyang University of Technology, Shenyang, China, 2006.

[3] H. Z. Cui and H. W. Yin, "New technology of plasma beam surface hardening on a cylinder," *Heat Treatment of Metals*, vol. 3, pp. 28-29, 2000.

[4] L. J. Yang, "The effect of specimen thickness on the hardness of plasma surface hardened ASSAB 760 steel specimens," *Journal of Materials Processing Technology*, vol. 185, no. 1-3, pp. 113–119, 2007.

[5] I. Etsion, "State of the art in laser surface texturing," *Journal of Tribology*, vol. 127, no. 1, pp. 248–253, 2005.

[6] S. F. Huang, "Laser surface hardening treatment of medium carbon chromium-molybdenum steel AISI4140," *Journal of china university of science and technology*, vol. 50, 2012.

[7] H. Q. Chen, *Research on Laser Surface Hardening of Tool Steel*, Master's degree thesis, Institute of Materials Science and Engineering, National Dong Hwa University, Taiwan, 2003.

[8] F. Lusquiños, J. C. Conde, S. Bonss et al., "Theoretical and experimental analysis of high power diode laser (HPDL) hardening of AISI 1045 steel," *Applied Surface Science*, vol. 254, no. 4, pp. 948–954, 2007.

[9] E. J. N. L. Silva, J. F. N. Giraldes, C. O. de Lima, V. T. L. Vieira, C. N. Elias, and H. S. Antunes, "Influence of heat treatment on torsional resistance and surface roughness of nickel-titanium instruments," *International Endodontic Journal*, vol. 52, no. 11, pp. 1645–1651, 2019.

[10] Y.-C. Lin, H.-M. Chen, and Y.-C. Chen, "Analysis of microstructure and wear performance of SiC clad layer on SKD61 die steel after gas tungsten arc welding," *Materials & Design*, vol. 47, pp. 828–835, 2013.

[11] L. W. Tasy, Z. W. Lin, R. K. Shiue, and C. Chen, "Hydrogen embrittlement susceptibility of laser-hardened 4140 steel," *Materials Science and Engineering A*, vol. 290, pp. 46–54, 2000.

[12] Y. Rong, X. Zuo, and N. Chen, "Clean water-air alternative timed quenching (ATQ) technology: principle and applications," *Jinshu Rechuli/Heat Treat Met.*vol. 43, no. 4, pp. 1–9, 2018.

[13] U. Koklu, "The drilling machinability of 5083 aluminum under shallow and deep cryogenic treatment," *Emerging Materials Research*, vol. 9, no. 2, pp. 323–330, 2020.
[14] K. . Uğur, S. Morkavuk, and L. Urtekin, "Effects of the drill flute number on drilling of a casted AZ91 magnesium alloy," *Materials Testing*, vol. 61, no. 3, pp. 260–266, 2019.
[15] T. Dharmen, K. N. Srinivasan, S. A. Channiwala, and M. S. M. Panwala, "Simulation of temperature field of TIG welding using FDM," *ASME*, in *Proceedings of the Pressure Vessels and Piping Conference*, Las Vegas, Nevada, USA, July 2009.
[16] K. Komvopoulos, *Mechanical Testing of Engineering Materials*, University of California, Berkeley, Cognella, 2011.
[17] M. Abreu, J. Sundberg, J. Elfsberg, and S. Jonsson, "Morphology and mechanisms of cavitation damage on lamellar gray iron surfaces," *Wear*, vol. 456-457, p. 15, 2020.
[18] I.-C. Park, H.-K. Lee, and S.-J. Kim, "Microstructure and cavitation damage characteristics of surface treated gray cast iron by plasma ion nitriding," *Applied Surface Science*, vol. 477, pp. 147–153, 2019.
[19] N. H. Jung, J. H. Ahn, M. J. Lee, N. H. Kang, and K. M. Cho, "Formation behavior of δ ferrite within LB and GTA weld zones of mod. 9Cr-1Mo steel in terms of thermal history," *Korean Journal of Metals and Materials*, vol. 56, no. 2, pp. 93–102, 2019.
[20] W. Zhongyin, D. Liguang, and X. Faren, "Study of heat conduction mathematic model of plasma hot machining," *Journal of Guangxi Institute of Technology*, vol. 5, no. 4, pp. 45–50, 1994.
[21] H.-Y. Bor, *A Study on the Elevated Temperature Brittleness and Fracture Mechanism of Mar-M247 Super-Alloy*, National Chiao Tung University, Hsinchu, Taiwan, 1998.
[22] S. H. Chen and K. T. Tsai, "Predictive analysis for the thermal diffusion of the plasma-assisted machining of superalloy inconel-718 based on exponential smoothing," *Advances in Materials Science and Engineering*, vol. 2018, Article ID 9532394, 2018.
[23] Y. S. Jiang, *Machinery Materials II*, National Taiwan University of Science and Technology Books, 2018.
[24] G. X. Liu, *Engineering Materials Science*, Quanhua Books, Taipei, Taiwan, 2014.
[25] M. Ohring, *Engineering Materials Science*, Academic Press, Cambridge, MA, USA, 1st edition, 1995.
[26] J. L. Dong, *Steel Material*, Sanmin Publishing House, Beijing, China, 1985.
[27] A. Dean, D. Voss, and D. Draguljić, "Response surface methodology," in *Design and Analysis of Experiments*, pp. 565–614, Springer Texts in Statistics, Springer, Cham, Switzerland, 2017.
[28] R. R. Barton, "Response surface methodology," *Encyclopedia of Operations Research and Management Science*, pp. 1307–1313, 2016.
[29] C. D. Lewis, *Industrial and Business Forecasting Methods*, Butterworth, London, UK, 1982.
[30] A. Shokri, "Application of Sono-photo-Fenton process for degradation of phenol derivatives in petrochemical wastewater using full factorial design of experiment," *International Journal of Integrated Care*, vol. 9, no. 4, pp. 295–303, 2018.
[31] S. H. Chen and B. T. Wang, "Development research on integrating CNC machine tool with plasma for on-line surface heat treatment," *Preprints*, Article ID 2021060583, 2021.